APPLIED SCIENCES AND ENGINEERING

Soft electromagnetic actuators

Guoyong Mao[1,2]*, Michael Drack[1,2†], Mahya Karami-Mosammam[1,2†], Daniela Wirthl[1,2], Thomas Stockinger[1,2], Reinhard Schwödiauer[1,2], Martin Kaltenbrunner[1,2]*

Rigid electromagnetic actuators serve our society in a myriad of ways for more than 200 years. However, their bulky nature restricts close collaboration with humans. Here, we introduce soft electromagnetic actuators (SEMAs) by replacing solid metal coils with liquid-metal channels embedded in elastomeric shells. We demonstrate human-friendly, simple, stretchable, fast, durable, and programmable centimeter-scale SEMAs that drive a soft shark, interact with everyday objects, or rapidly mix a dye with water. A multicoil flower SEMA with individually controlled petals blooms or closes within tens of milliseconds, and a cubic SEMA performs programmed, arbitrary motion sequences. We develop a numerical model supporting design and opening potential routes toward miniaturization, reduction of power consumption, and increase in mechanical efficiency. SEMAs are electrically controlled shape-morphing systems that are potentially empowering future applications from soft grippers to minimally invasive medicine.

INTRODUCTION

Robots are entering our daily life in many different fields, ranging from industrial production, autonomous transport, public security, and personal assistants to medical applications. Consequently, they are getting physically closer and closer to our human body. For instance, the use of robots to perform surgery guided by magnetic resonance imaging (MRI) (*1*, *2*) is currently considered. For future applications similar to this, safe interaction between robots and the human body becomes a necessity. Since M. Faraday demonstrated the first rudimentary electric motor in 1821, the designs of the electromagnetic motors that form the core parts of conventional robots have undergone numerous changes. Still, the vast majority of conventional electric motors is made solely from hard materials such as copper or iron. The interplay of numerous rigid parts is necessary to accomplish complex tasks but renders these devices harmful when operated in the vicinity of the human body or fragile objects (*3*). This major drawback of conventional robotics drives the development of new soft functional actuators that are sensitive to various triggers ranging from heat, humidity, pH, light, and pressure to electric or magnetic fields (*4*–*12*).

However, current soft functional actuators meet limitations in real-life applications such as slow response time or low power, are difficult to control precisely, or require dangerous stimuli (e.g., high voltage) (*4*–*7*). For example, while dielectric elastomer actuators show good mechanical performance (*9*, *13*–*15*), their actuation voltage typically exceeds thousands of volts and poses a risk for humans. Pneumatic fluidic actuators are widely used in soft robotics and even in rehabilitation equipment due to their ability to generate large force (*10*, *16*) but need high-pressure equipment (>300 kPa) and are slow in response (<0.5 Hz) (*16*). Untethered soft magnetic robots consisting of elastomers with ferromagnetic fillers are readily miniaturized and powered wirelessly, rendering them a good candidate for biomedical applications (*12*, *17*, *18*). However, they only allow few, specifically designed movements after fabrication (*18*). Compared to current soft functional actuators, conventional electromagnetic motors still offer many advantages such as fast response and lower actuation voltage, as well as highly programmable and well-controlled movements.

By reforming structure and materials, new types of soft electromagnetic actuators (SEMAs) become available (*19*, *20*). The basic designs presented so far are similar to conventional loudspeakers, replacing the copper wires with liquid-metal coils. In these designs, the liquid-metal coils are pulled and pushed by the Lorentz force, which is mainly generated by the radial magnetic field component B_R. As B_R is almost zero at the center of the magnet and large around the boundary, the size of the liquid-metal coil should be larger than that of the magnet. This limits the miniaturization, performance, and multifunctionality of the actuators exposed to a weak magnetic field of a small magnet. Furthermore, since B_R decreases fast with the distance from the surface of the magnet, it is essential to reduce the distance between actuator and magnet. Unlike in (*19*), where the magnet is connected to the liquid-metal coil, the actuators in (*20*) consist of a solid frame holding the magnet. The solid bonding between the permanent magnet and the coils, in both cases, prevents these actuators from becoming fully soft.

Decoupling of (rigid) magnets and soft actuators increases the application space. For example, in medical surgical robots, an MRI machine enables the navigation necessary for the surgery and, in addition, provides a strong magnetic field in the human body. This approach could potentially establish SEMAs as an alternative to conventional electromagnetic motors and robots in the field of medical applications such as in minimally invasive medicine. Here, we present several design strategies and a set of methods to fabricate high performance and fully soft electromagnetic actuators to power soft forms of robotics. We now explore the six main design strategies of our SEMAs:

1) A large plate magnet is used that provides a spatially extended and strong magnetic field, allowing us to separate the SEMAs from the rigid magnet, thus rendering them fully soft.

2) The distribution of the magnetic field of the plate magnet is characterized and modeled. This allows predicting the mechanical response of the actuator using a numerical model developed for this purpose and, in turn, provides guidelines to enhance the performance of our SEMAs.

[1]Division of Soft Matter Physics, Institute for Experimental Physics, Johannes Kepler University Linz, Altenberger Strasse 69, 4040 Linz, Austria. [2]Soft Materials Lab, Linz Institute of Technology, Johannes Kepler University Linz, Altenberger Strasse 69, 4040 Linz, Austria.
*Corresponding author. Email: guoyong.mao@jku.at (G.M.); martin.kaltenbrunner@jku.at (M.K.)
†These authors contributed equally to this work.

3) The use of rectangular coils results in a larger magnetic torque compared to circular ones.

4) Our SEMA design defines the plane of the coil perpendicular to the surface of the plate magnet, thus increasing the out-of-plane Lorentz force.

5) A cost-efficient molding method is used to manufacture the SEMAs. This easy to customize fabrication method provides thick liquid-metal channels that enable higher driving currents.

6) Multiple coils are used in our SEMAs to increase the force output and the degrees of freedom.

To compare our SEMAs with traditional DC motors, we illustrate their typical structures in fig. S1. Conventional DC motors mainly consist of a stator, a rotor, a commutator, and a pair of electric brushes (fig. S1A). Our new class of SEMAs innervates these designs by replacing the hard-rigid parts and structures with liquid-metal channels embedded in a soft elastomer shell. In addition, a plate-permanent magnet serves as a magnetic field source similar to a stator. Different from conventional DC motors, our SEMAs are softer with fewer parts and, consequently, may offer advantages in miniaturization and robustness as fewer components are prone to mechanical failures. The working principle is schematically illustrated in Fig. 1A. The single-coil square SEMA arranged in the setup (fig. S1B) will bend when a current is sourced through the conductive channel due to the Lorentz force. Such a SEMA can be directly used as a motor for soft robotics rather than passing the force through links and gears, as required by conventional DC motors. The driving voltage is below 1 V and, hence, harmless to humans and even allows for underwater operation. We demonstrate this with a swimming soft shark (Fig. 1B, fig. S2, and movie S1) where SEMAs act as tail and fins.

RESULTS

Considering fundamental physical principles, SEMAs can be modeled as a series of conductive wires in a magnetic field. The driving force is thus calculated according to the Lorentz force law, $\mathbf{F} = \mathbf{I} \int dl \times \mathbf{B}$, where $\mathbf{I}$ is the current passing through the wire, dl is an infinitesimal segment of the wire, and $\mathbf{B}$ is the magnetic flux density. Understanding the distribution of the magnetic field is essential for the design and actuation of SEMAs. In the experiment, we use a plate magnet (fig. S3A) to generate an axisymmetric magnetic field (fig. S3B). The quantitative magnetic field is characterized by experiment and simulation (fig. S3, C to I) and can be fitted with a set of analytical equations (see Materials and Methods). The operating principle dictates that higher currents result in larger forces. However, high currents cause stronger joule heating, implying that low electrical resistance is required for the SEMA. We achieve this using liquid metals as the stretchable conductor, in conjunction with a proper design of the channel dimensions. While larger channels are a straightforward way to reduce resistance, the distribution of the magnetic field as given by the plate magnet sets an upper boundary. Balancing all factors, we set the dimensions of the channels to a thickness of 0.5 mm and a width of 1 mm. There are numerous ways to fabricate liquid-metal channels in elastomers based on microfluidics (*21*). Here, we use molding as a frugal approach. The entire fabrication process is depicted in Fig. 1C. Via this simple, scalable fabrication method, we achieve precisely patterned elastomers (fig. S4, A to D) and well-sealed liquid-metal channels (fig. S4, E and F, and movie S2).

In actuation, our SEMAs accomplish bending as specified by their design (fig. S5, A and B) as one end of the SEMA is fixed. We predict the bending moment applied to the SEMA by theory, as shown in fig. S5B. For example, the bending moment is 0.88 mN·m

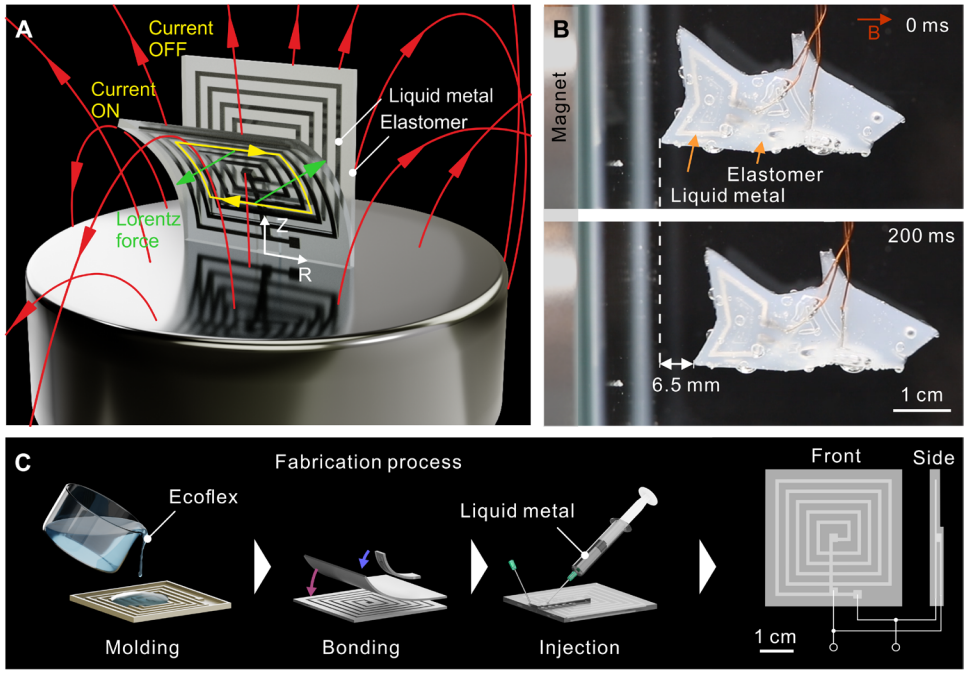

Fig. 1. Working principle and fabrication process of SEMAs. (**A**) Schematic working principle of a SEMA subjected to a current load in a magnetic field. (**B**) A swimming soft shark driven by SEMAs (tail and fins; movie S1). (**C**) Main steps of the SEMA fabrication: molding of the silicone elastomer, bonding to a sheet of elastomer to fabricate channels, and, last, injection of the liquid metal. Front and side layout of the finished square SEMA with both ends of the liquid metal connected to a control system. (Photo Credit: Michael Drack and Guoyong Mao/Johannes Kepler University Linz).

when the SEMA is driven by a current of 3 A (DC). We verified the current-dependent bending movement of a single-coil square SEMA via well-matching simulations and experiments (Fig. 2, A and B). The numerical model is described in more detail in Materials and Methods (fig. S5, C to F).

In the experiments, the single-coil square SEMA can bend more than 70° with a 3-A current (DC). The experiments reveal a linear relationship between the maximum rotation angle and the applied current up to 5 A (Fig. 2C). In the simulation, we can increase the current up to 10 A, resulting in a maximum rotation angle approaching 105° (Fig. 2C) for currents larger than 5 A. The final rotation angle cannot reach higher values due to the principal direction of the Lorentz force always being horizontal (fig. S5B) as a consequence of the magnetic field distribution ($B_R >> B_Z$). We obtain the strain energy of the SEMA versus the current from simulation (fig. S6A). The strain energy increases almost linearly with increasing current and reaches 3 mJ at 10 A. Considering the weight of the SEMA, 7.5 g (elastomer, 6.0 g; liquid metal, 1.5 g), the maximum energy density is 0.4 mJ/g, which is roughly $^1/_{10}$ that of human muscles [about 3.6 mJ/g (*22*)]. Here, when calculating the energy density or later power density, only the mass of the elastomer shell and the liquid metal is taken into account, the mass of the magnet is not considered [in line with other types of magnetic soft actuators where, i.e., Helmholtz coils serve as magnetic field sources (*17*)].

The lower energy density is a consequence of the high mass density of the liquid metal (6.44 g/cm^3; six times more than that of natural muscle, which is about 1 g/cm^3), the low magnetic field of the stator magnet (average, <300 mT; fig. S3), and the resistivity of the liquid metal. We gauge methods on how to increase the energy density and therefore further improve the performance of the SEMA by developing a simplified model. It is considered that the current passes only through the top horizontal channel of the SEMA

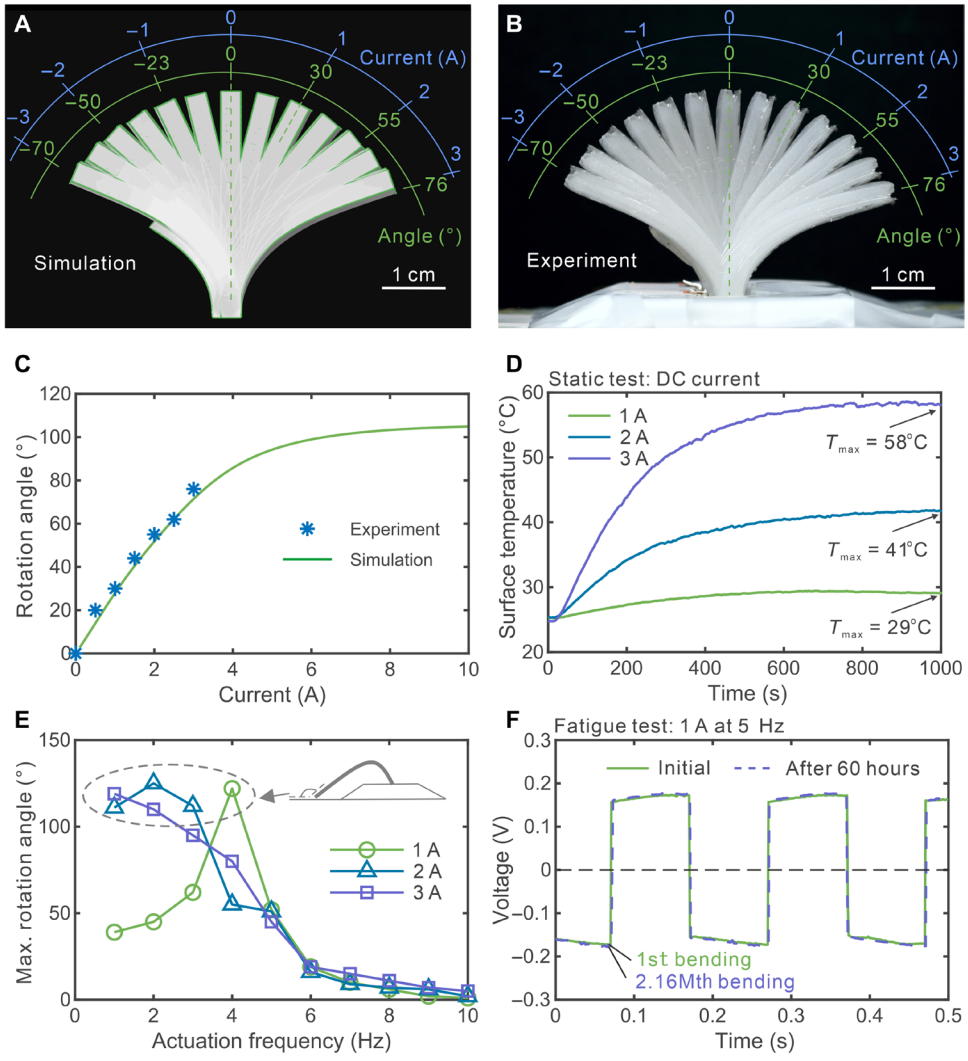

Fig. 2. Characterization of a single-coil square SEMA. Rotation angle of the SEMA subjected to a DC current from 1 to 3 A (**A**) predicted in the simulation and (**B**) observed experimentally (movie S3). (**C**) Rotation angle of the SEMA as a function of the current for experiment and simulation. (**D**) Temporal change of the surface temperature of the SEMA for three specific values of DC current, 1, 2, and 3 A. (**E**) Maximum rotation angle of the bending SEMA subjected to square wave currents, with varying amplitude and frequency. Inset: Maximum rotation angle is limited by the actuator touching the ground. (**F**) Fatigue test with 5 Hz at a current of 1 A. Comparison of the voltage drop versus time at the beginning and the end of the test shows a perfect overlap of the first and the 2.16Mth bending cycle, evidencing the high durability of the SEMA. (Photo Credit: Michael Drack and Guoyong Mao/Johannes Kepler University Linz).

(fig. S6B), and the whole SEMA acts as a linear elastic beam under pure bending. Then, the strain energy obeys the relationship $W \sim B^2I^2$ and, thus, scales quadratically both with the magnetic field and a driving current. A commercial MRI machine can generate a magnetic field of 7 T (MAGNETOM Terra, SIEMENS), which is 35 times larger than the fields used in our experiments (on average, about 200 mT). These strong fields (7 T) will increase the strain energy by a factor of $35^2 = 1225$, far exceeding the value of natural muscle.

A second option to improve the strain energy of the SEMA is to increase the amplitude of the current. However, joule heating effects then result in an increase in heat and temperature. Experimental results yield that 70°C is the maximum temperature that our single-coil square SEMA can resist. Therefore, the joule heating power, $P_{heat} = I^2R$, should be considered when designing a SEMA. We conduct a series of temperature tests to determine the maximum (equilibrium) temperature of the SEMAs subjected to a static test (DC current) and a dynamic test with the same amplitude and an effective current of 1, 2, and 3 A (Fig. 2D and fig. S6, C and D). Because of the low, actuation-independent resistance of the SEMA (0.18 ohm) (fig. S6, E and F), the maximum temperature reached is only 58°C, with a constant 3-A current applied. The temperatures in dynamic tests are even 12°C lower than those in static tests, which results from an enhanced heat exchange between the SEMA and the environment, considering the same heat power in the two tests. Pulsed operation or active cooling systems allow higher current amplitudes that we have tested (25 A, 100-ms pulses). The heat power $P_{heat} = I^2R$ is 1.62 W with 3 A, which can be used as a design rule for the same geometry of the SEMA. Considering the limitation of $P_{heat,}$ the maximum strain energy of the SEMA can be written as $W_{max} \sim B^2/R$. Therefore, a decrease in the resistance of the SEMA is directly linked to an increase in performance. We note that the resistivity of liquid metal can be 1.67×10^{-7} ohm · m by adding highly conductive particles such as copper (*23*). This would increase the maximum strain energy density by 73%. By analysis, the number of turns of the coil will not affect the maximum strain energy density of the SEMA with the temperature limit given by the joule heating (details in the Supplementary Materials).

We conduct a series of actuation frequency tests to investigate the dynamic performance of our SEMAs. Excitation of the single-coil square SEMA at frequencies from 1 to 10 Hz reveals peaks in the measured maximum rotation angle (Fig. 2E). This mechanical resonance behavior at lower frequencies is common for soft robots and found, for example, for dielectric elastomer actuators (*24*). At a current of 1 A, the resonance frequency is close to 4 Hz, resulting in a strongly elevated maximum rotation angle (Fig. 2E), with the SEMA almost touching the ground. An increase in current leads to a shift of this resonance to lower frequencies. Applying very high frequencies of up to 8192 (2^{13}) Hz with a current of 3 A (movie S4) demonstrates the applicability of SEMAs for loudspeakers similar to the ones found in the literature (*19*). Prolonged fatigue tests (actuation at a frequency of 5 Hz for 60 hours) show that a single-coil square SEMA bends over 2.16 million times to a maximum rotation angle of 61° without any change in performance (Fig. 2F and fig. S6G).

Miniaturization of SEMAs seems straightforward, as there are various methods to fabricate microsize liquid-metal channels available (*25*). Practical limitations (stemming, i.e., from large currents used) are analyzed here using numerical simulations, providing insight on the scalability and efficiency of SEMAs. For the simulation, a single-coil square SEMA is taken as a reference actuator (Fig. 2B). To investigate the scalability, we assume that α is the scale factor of the actuator, with α times the size of the reference actuator (40 mm by 40 mm by 3.5 mm). The resistance of the scaled SEMA can be expressed as $R = \rho l_{RC}/(\alpha S_{RC})$, where l_{RC} and S_{RC} are the length and cross-section area of the liquid-metal channels of the reference actuator, respectively. The heat power generated by the SEMA is calculated as $P_{heat} = I^2R$. The maximum power of the heat dissipation is proportional to the surface area of the actuator, $P_{dmax} \sim \alpha^2 S_{RA}$, where S_{RA} is the area of the front plus the back surface of the reference actuator, neglecting the surface along the thickness direction. If $P_{heat} = P_{dmax}$, then we obtain a relationship between the maximum current and the scale ratio as $I_{smax}^2 = \alpha^3 I_{Rmax}^2$, where $I_{Rmax} = 3$ A is the maximum current that we tested with the reference actuator (Fig. 2A). In the simulation, the setup is similar to that in Fig. 2B but with a homogenous magnetic field $B = 400$ mT that is readily available using large permanent magnets. Considering that the heat-transfer coefficient of water is a thousand times that of air and the relation $I_{smax}^2 = \alpha^3 I_{Rmax}^2$, we multiply the maximum current by 10, resulting in a moderate current of $I = 10\ I_{smax}$. Figure S7 shows the relationship between current and heat-power consumption of scaled SEMAs to reach bending angles from 10° to 90°. According to the simulation, both the current and the heat power necessary to reach a specific bending angle are decreasing with the decline of the scale factor. For example, a maximum angle of about 30° is achieved with a current of 1 mA for a scale factor $\alpha = 0.001$ (fig. S7A), and the heat power is about 0.13 mW (fig. S7B) and, therefore, much lower in comparison with the reference actuator.

To evaluate the mechanical efficiency of the SEMAs, we apply a pulse current (fig. S8A) to various scaled single-coil square actuators. The mechanical efficiency of the SEMA can be calculated as $\eta = E_w/(E_w + Q)$, where Q can be calculated as $Q = I^2Rt$ (fig. S8A). The work E_w performed by the actuator is calculated with a dynamic numerical model. The work E_w consists of two parts, namely, the strain energy E_s and the kinetic energy E_k (fig. S8B). In fig. S8C, the mechanical efficiency first increases and then decreases until it reaches a maximum value around the time when the kinetic energy reaches its maximum value. By calculating the mechanical efficiency for SEMAs with different scale factors, we find that the mechanical efficiency for $\alpha = 0.1$ compared to $\alpha = 1$ drops from 4.2 to 0.5% with the same I_{smax} (fig. S8D) and for $\alpha = 0.01$ (0.4 mm by 0.4 mm by 0.035 mm), it is around 1.7×10^{-5}. In weak magnetic fields, microsize SEMAs are thus not practicable for real applications due to their low efficiency, implying different designs or a stronger magnetic field (>400 mT, for example, supplied by an MRI machine) are required.

To estimate the efficiency, a simple theoretical model is given in the Supplementary Materials. We find that an increase in the actuation velocity of the liquid-metal channels will result in an increase in efficiency. Starting from the dimensions of the reference actuator, we reduce the thickness of its shell from 3.5 to 2.5 mm, consequently lower its bending stiffness, and thus enhance its rotation speed. Numerical results yield that mechanical efficiency increases from 4.2 to 4.8% at $I = I_{smax}$ and from 10 to 19% at $I = 0.1\ I_{smax}$ (fig. S8E). Similarly, an increase in the magnetic field results in an increase in the mechanical efficiency according to the theoretical prediction. The mechanical efficiency of a 2.5-mm-thick single square actuator, for instance, is close to 80%, with a magnetic field of 1.6 T and nearly 100% with a magnetic field over 4 T (fig. S8F).

To determine the power of the SEMAs, we build a double-coil square one (fig. S9), providing a higher force than the single-coil version. In Fig. 3A, the SEMA is connected to a weight with a thread via a deflection pulley. Measuring the trace of the weight gives its time-dependent displacement curve and, consequently, speed and acceleration, which are used to calculate the power and efficiency (Fig. 3, B to D). The maximum output power of the SEMA is about 57 mW, and the maximum power density is about 5.3 mW/g. Applying a 1-Hz sine-wave current with three different amplitudes of 1, 2, and 3 A results in efficiencies of 0.36, 0.21, and 0.15%, respectively. This is consistent with previous simulation (fig. S8C) in which as the time increases, the efficiency decreases and the efficiency decreases as the current increases (fig. S8D). Most of the power (>99%) is dissipated in the form of heat to the environment (fig. S10).

On the basis of the above performance analysis, SEMAs are capable of particular movements (such as fast periodic bending) that are difficult to achieve for other types of soft functional actuators. We designed several types of SEMAs and presented their specific skills in tailored demonstrations. In Fig. 3E, a double-coil square SEMA hits a ping-pong ball hanging on a thread similar to a simple pendulum. By applying a current pulse (−3 to +3 A), the SEMA pushes the ball 47 mm into the air, wherein it transfers at least 1.2 mJ of mechanical energy to the object. With a square wave current of 1 A at 1.5 Hz, the SEMA hits the ball periodically (playing ping-pong; fig. S11 and movie S6). We demonstrate underwater operation with a fish tail–like SEMA (fig. S12A), i.e., serving as a motor for swimming robots (Fig. 1B). In contrast to dielectric elastomer–based soft actuators that typically require several thousand volts, our SEMAs work with a voltage four orders of magnitude lower (<1 V), which enables safe operation even when immersed in water without requiring sophisticated isolation barriers. We place the fish-tail SEMA at the bottom of a water tank, with a plate magnet underneath the tank (fig. S12B). Applying a 3-A square wave current lets the fish-tail SEMA swing very much like a real fish tail (Fig. 4A and movie S7) and speeds up the mixing of a blue dye dripped into water (Fig. 4B and movie S7). The video depicts the vortex-induced by the SEMA and indicates high performance (Fig. 4B).

Apart from single-coil SEMAs, we develop multicoil ones to show their high programmability. There are various flower-shaped actuators made of other soft functional materials, such as shape-memory polymers, pH-sensitive hydrogels, or magnetic polymers, as well as pneumatically driven actuators (*26*–*29*). However, most of these actuators only allow for two switching states, fully open or closed as a whole. We here develop a multicoil flower SEMA assembled from five SEMAs each acting individually as one petal (Fig. 4C and fig. S13, A and B). When designing the petals, it is essential to identify a proper shape and suitable thickness to ensure the complete closing and opening of the flower actuator. To get a large magnetic torque, we continue to use rectangular coils instead of circular ones (fig. S13A). At its initial state (without current), the flower is resting

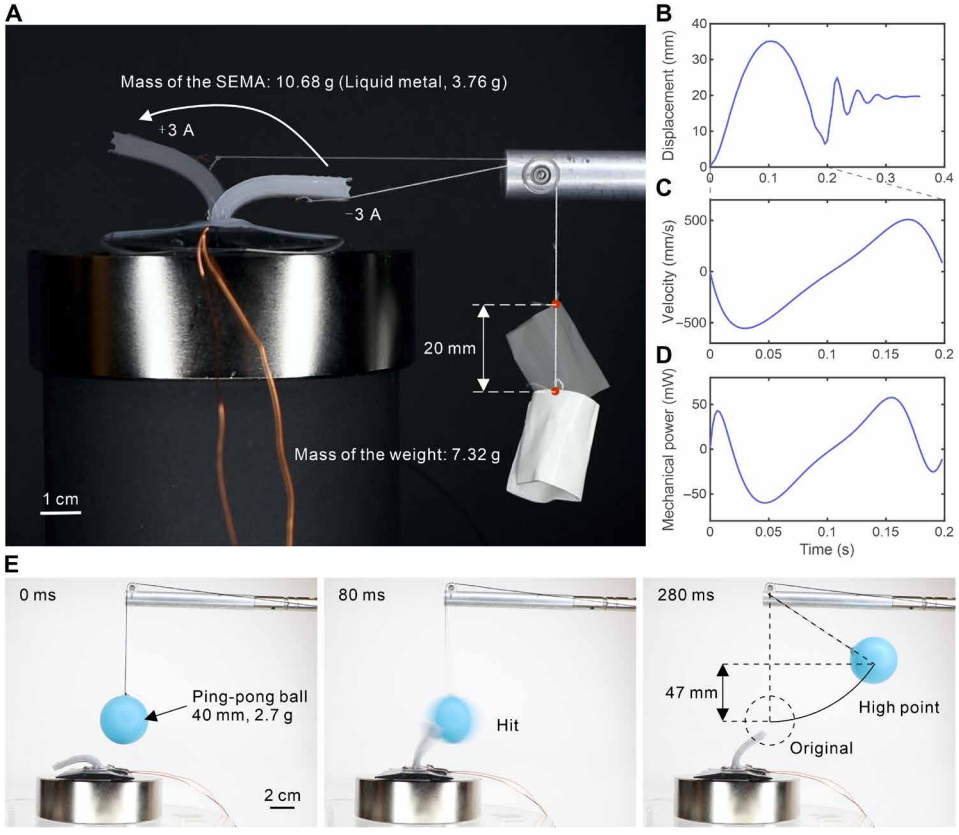

Fig. 3. Power and efficiency of a double-coil square SEMA. (**A**) Experimental setup for the power and efficiency test. By switching the DC current from −3 to 3 A, the SEMA bends from one to the other side and lifts the weight by 2 cm via a deflection pulley (movie S5). (**B**) Displacement of the SEMA responding to the sudden current change from −3 to 3 A. (**C** and **D**) The velocity and mechanical power response of the SEMA over time in the initial 0.2 s after switching the current. (**E**) A double-coil square SEMA hits a ping-pong ball mounted on a string 47 mm into the air (movie S6). (Photo Credit: Michael Drack and Guoyong Mao/Johannes Kepler University Linz).

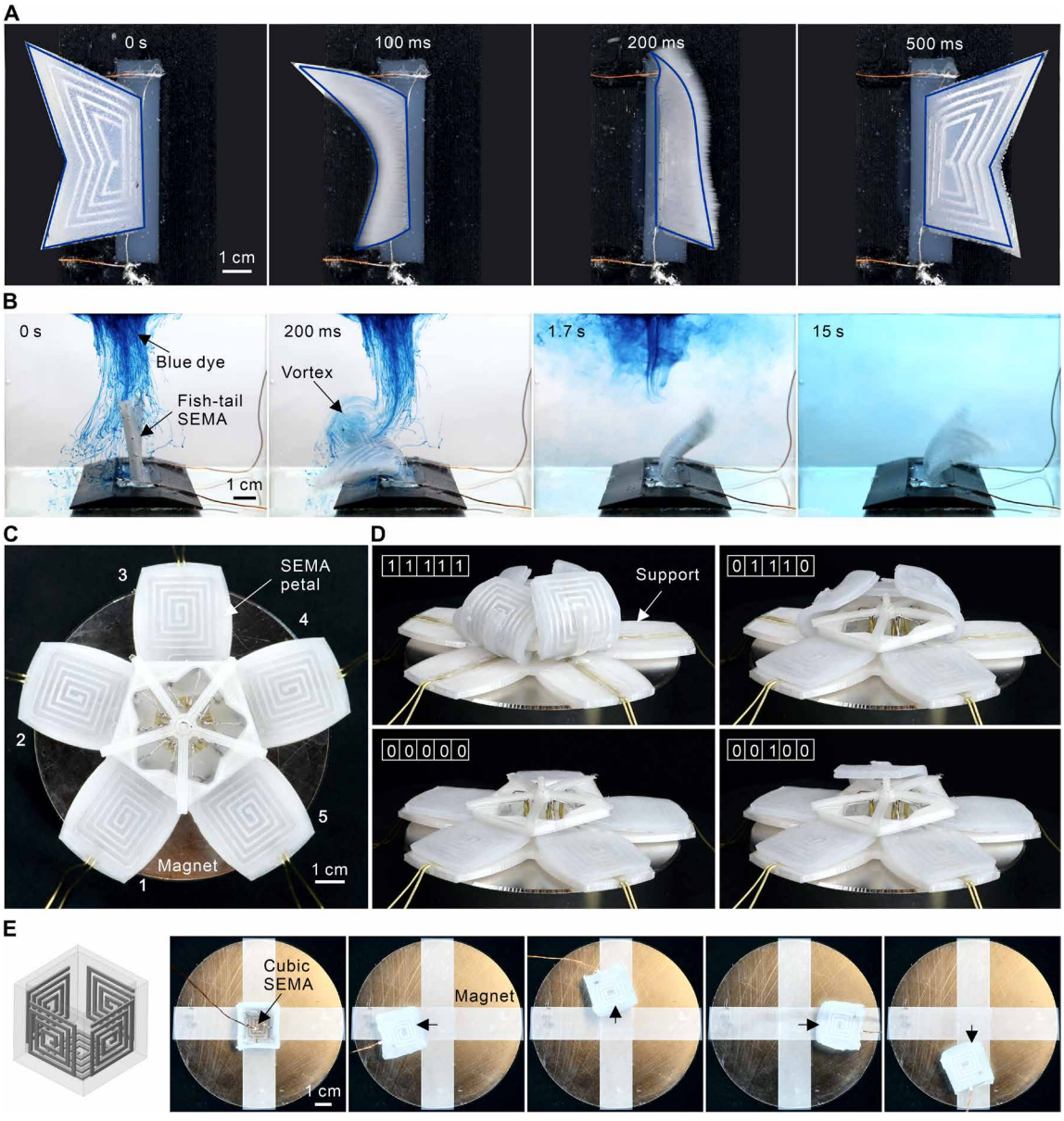

Fig. 4. Functionalities of SEMAs. (**A**) Dynamic swinging of a fish-tail SEMA (top view; movie S7). (**B**) Fish-tail SEMA as a blender speeding up the mixing of blue dye and water (movie S7). (**C**) Flower SEMA (top view). The five petals are numbered from 1 to 5. The elastomer support joining the five SEMAs to one flower is described in fig. S11B. (**D**) Flower SEMA in different actuated modes (movie S8). Each bit of the binary number represents the on- (1) or off-state (0) of a single petal corresponding to the numbers in (C). (**E**) Design and operation of a cubic SEMA and its rotation subjected to different current signals (movie S9). (Photo Credit: Michael Drack and Guoyong Mao/Johannes Kepler University Linz).

at the center of the top surface of the magnet, and the coils of all petals are positioned in parallel to the magnet, resulting in a Lorentz force mainly along the in-plane direction. Considering the distribution of the magnetic field (fig. S3), we choose the length of the petals to be close to the radius of the magnet. This design ensures that the magnetic field component B_R generates a magnetic torque large enough to bend the tips of the petal at the onset of the bending process (fig. S5). The following bending process is accomplished by the magnetic field component B_Z. Besides the length of the single petals, the thickness also affects the bending stiffness and its mass. If the petal is too thick, then the induced magnetic torque is not sufficient to bend the petal. If it is too thin, then the petal collapses, folds itself, and will no longer return to its initial position. In addition, we use the numerical model to study the dynamic response of the petals for different thicknesses (fig. S13C) subject to various current loads. This meticulous optimization of all parameters provides the experimental design space for flower-like SEMAs.

In contrast to other flower-shaped robots, our flower SEMA operates very fast, and each petal can be programmed individually (movie S8). The numbering of the petals (Fig. 4C) allows the use of a five-digit binary code to indicate the flower actuator's operational state (Fig. 4D). The individual petals can be programmed to close and open sequentially (fig. S14A) or simultaneously (fig. S14B), which enables the flower SEMA to hold objects such as a ball (fig. S14C). Full closing or opening of all five petals takes only 80 ms when applying a 5-A current (fig. S14, D and E), which is very fast

compared to other flower actuators, and for soft actuators in general. Closing and opening the petals one by one with time intervals of 10 ms, 50 ms, 100 ms, and 1 s show the outstanding dynamic performance of our SEMAs (movie S8).

If the liquid-metal coil is oriented perpendicular to the magnetic field, then only the in-plane forces act, and the SEMA will no longer bend. We suggest using three-dimensional (3D) liquid-metal coils to overcome this limitation. We build a cubic SEMA placed in the center of a plate magnet where $B_R >> B_Z$ to demonstrate the concept. Such a five-face cubic SEMA has one face open to allow connecting electrodes (fig. S15). By controlling the current through the cubic SEMA, it can rotate in any direction (Fig. 4E and movie S9). This design allows a SEMA to function in arbitrary magnetic fields.

DISCUSSION

In this study, on the basis of the principles of conventional electromagnetic actuators, we here introduce a series of SEMAs that actuate fast and are highly controllable (for a comparison with current popular soft actuators, see table S3). Their entirely soft body and low driving voltage (<1 V) render them innocuous when in contact with living organisms and fragile objects. The experimental and theoretical analysis predicts SEMAs with high energy density, power density, and efficiency if subjected to a strong magnetic field (available with a commercial MRI machine). Simulations indicate that the driving current and power consumption required for a 30° bending of single-coil SEMA drops from 0.56 A to 1 mA and from 57 to 0.13 mW, respectively, when reducing the size from centimeters to micrometers in a 400-mT magnetic field. The simulation also indicates that a 20% mechanical efficiency is possible with a permanent magnet and even close to 100% can be achieved with a 4-T magnetic field. Unlike conventional motors, our SEMAs are readily miniaturized because of their simple structure, the frugal fabrication process, and the wide availability of low-cost power electronics. Moreover, our SEMAs are well controlled and easily programmed, enabling individual actuation of soft robotic elements within more complex structures such as our flower SEMA. Our numerical and experimental analyses provide ample pathways to improve the power output and mechanical efficiency of SEMAs. New, lower-resistivity liquid-metal materials such as a Cu-EGaIn mixture (*23*) seem promising here. Equally, an increase in the number of turns of liquid-metal coils enhances the force and power output. Thinner actuators, albeit eventually challenging to realize and requiring new shell materials, will also enhance performance. The fabrication of small size and multicoil SEMAs is promising for the use of SEMAs in medical applications.

In the future, our work may translate into a multitude of use cases and revolutionize the development of advanced microrobots for medical applications (*30*) such as drug delivery, tissue diagnosis, and cell manipulation. In this way, the classic movie scene from *Fantastic Voyage* where a miniaturized submarine destroys a blood clot and saves the patient's life may one day become reality.

MATERIALS AND METHODS

Materials for SEMAs

SEMAs are made of a liquid metal embedded in a patterned soft elastomeric shell. The implemented liquid-metal Galinstan consists of gallium, indium, and tin with a mass ratio of 69:22:9 weight % (Smart Elements, smart-elements GmbH). The mass density and electrical resistivity of Galinstan are about 6.44 g/cm^3 and 2.89 × 10^{-7}ohm · m, respectively, at room temperature. The silicone elastomer for the elastic shell is fabricated from Ecoflex 00-30 (Smooth-on).

Characterization of the elastomer

The shear modulus of Ecoflex is obtained by a simple tension test, with a constant strain rate of 0.66%/s. The specimen geometry can be found in the European Standard EN ISO 527-2:1996 (type 5A). Fitting with the incompressible neo-Hookean hyperelastic model obtains the shear modulus of the Ecoflex, 49.12 kPa.

Fabrication of the SEMA

A 1:1 ratio of part A and part B of Ecoflex is mixed and degassed in a vacuum mixer system (DAC 600.2 VAC-P, Hauschild & Co. KG) (250 mbar for 1 min at 0 rpm, 350 mbar for 20 s at 1500 rpm, and 20 s at 2350 rpm). Subsequently, the uncured elastomer is poured into plastic molds and either cured at room temperature for 4 hours or in an oven at 65°C for 10 min, depending on the purpose. Molds for shell production are fabricated by 3D printing (Ultimaker 3 Extended, Ultimaker B.V.). The molded and readily cured elastomer films are bonded with uncured elastomer and fully cured in an oven at 65°C for half an hour. After the production of the elastomeric shell, the liquid metal is injected into the channels of the SEMA with a syringe (Fig. 1B). Two electrodes (tinned copper wire, no.390-549, RS Pro) are used to connect the SEMA with the control system. The electrodes are punctuated in the SEMA at the two ends of the liquid-metal channel. The punctuated sites are sealed with a thin elastomer layer processed according to the above bonding operation. The thickness of the SEMA is about 2.5 mm, including the two elastomeric sheets each 1 mm in thickness forming the shell, sandwiching the liquid-metal coil. The thickness of the liquid-metal coil is 0.5 mm, and the width of the liquid-metal channel is 1 mm. Dimensions and structure of a single-coil square SEMA are illustrated in fig. S4 (A to D).

Characterization of the magnet

The circular plate magnet (SM-100x30-N, magnets4you GmbH) is made of NdFeB (N45) and coated with nickel-copper-nickel. Its radius and height are 100 and 30 mm, respectively. We characterize the magnet with a Gauss meter (Gaussmeter HGM09s, Goudsmit Magnetic Systems). The magnetic field strength in the Z direction is measured by the Gauss meter at a distance of 6 mm to the surface of the magnet. Multiple positions on top of the magnet are measured as shown in fig. S3C. The measured magnetic field strength is used to fit the remanent magnetization. We use the commercial finite-element package COMSOL to obtain the distribution of the magnetic field. In the simulation, we assume that the magnet material is homogenous and axisymmetric in geometry. Combining experiment and simulation, we obtain the remanent magnetization of the plate magnet, 1.31 T.

The distribution of the magnetic field is shown in fig. S3 (E to I). We can find a cylinder (R ~ 20 mm and Z ~ 50 mm) on top of the plate magnet in which the magnetic field is mainly in Z direction and the magnetic field amplitude in R direction is negligible. We can fit these amplitudes at $R = 0$ along the Z direction, which shows a linear behavior with $B_Z = -5.2485 \times Z + 343.4$ (mT). This results in a magnetic space with $B_R = 0$ and B_Z on top of the plate magnet.

On the basis of the simulation, we further obtain a group of 2D polynomials to express the whole magnetic field

$$B_R = \sum_{i=0}^{i=5}\sum_{j=0}^{j=5} P_{ij} R^i Z^j, (i+j \le 5) \quad (1)$$

$$B_Z = \sum_{i=0}^{i=5}\sum_{j=0}^{j=5} Q_{ij} R^i Z^j, (i+j \le 5) \quad (2)$$

Fitting with these 2D polynomials via MATLAB yields the values for the parameters P_{ij} and Q_{ij} listed in table S1. The comparison of the fitted magnetic field resulting from the 2D polynomials with the magnetic field from the simulation is plotted in fig. S3 (H and I), proofing good agreement both in Z and R directions. Last, we input these 2D polynomials in the commercial finite-element method software ABAQUS for the mechanical simulation.

Numerical simulation

We simulate the mechanical response of the SEMAs with the finite-element software ABAQUS. To describe the mechanical behavior of the elastomer, we use an incompressible Neo-Hookean hyperelastic model with a shear modulus of 49.12 kPa. The inhomogeneous magnetic field predicted by Eqs. 1 and 2 is implemented to the simulation by the subroutine UTRACLOAD. We use a surface traction force to represent the Lorentz force via the same subroutine, as it is not possible to apply such a Lorentz force directly in ABAQUS. The directions of the surface traction forces can be determined according to the loading condition (fig. S5, C and D). In fig. S5 (E and F), we show a loading condition that is implemented in the simulation. In addition, we can describe the surface traction force per unit area on the channels with $p = IB_Z \sin\theta/w$, where θ is the angle between the magnetic field and the current direction (usually $\theta = \pi/2$) and w is the width of the liquid-metal channel.

Control and power systems

Two different control systems were used for the experiments. One is a self-built voltage to current converter for sourcing a current (0 to 3 A), corresponding to an input voltage signal provided by a waveform generator (Agilent 33250A, Keysight Technologies). The other one is a multichannel pulse-width modulation (PWM) voltage-control system consisting of a microcontroller (Arduino Uno Rev3), a 16-channel PWM controller (PCA9685, Adafruit), and five PWM output stages (BTS7960B, JKZ) for providing five separate PWM signals. Both control systems are connected to a power supply (PS-2403D, Voltcraft or PE 1645, Philips).

SUPPLEMENTARY MATERIALS

Supplementary material for this article is available at http://advances.sciencemag.org/cgi/content/full/6/26/eabc0251/DC1

REFERENCES AND NOTES

1. D. Stoianovici, D. Song, D. Petrisor, D. Ursu, D. Mazilu, M. Mutener, M. Schar, A. Patriciu, "MRI stealth" robot for prostate interventions. *Minim. Invasive Ther. Allied Technol.* **16**, 241–248 (2007).
2. W. Neumann, T. P. Pusch, M. Siegfarth, L. R. Schad, J. L. Stallkamp, CT and MRI compatibility of flexible 3D-printed materials for soft actuators and robots used in image-guided interventions. *Med. Phys.* **46**, 5488–5498 (2019).
3. G. M. Whitesides, Soft robotics. *Angew. Chem. Int. Ed. Engl.* **57**, 4258–4273 (2018).
4. J. Mu, M. Jung de Andrade, S. Fang, X. Wang, E. Gao, N. Li, S. H. Kim, H. Wang, C. Hou, Q. Zhang, M. Zhu, D. Qian, H. Lu, D. Kongahage, S. Talebian, J. Foroughi, G. Spinks, H. Kim, T. H. Ware, H. J. Sim, D. Y. Lee, Y. Jang, S. J. Kim, R. H. Baughman, Sheath-run artificial muscles. *Science* **365**, 150–155 (2019).
5. H. Arazoe, D. Miyajima, K. Akaike, F. Araoka, E. Sato, T. Hikima, M. Kawamoto, T. Aida, An autonomous actuator driven by fluctuations in ambient humidity. *Nat. Mater.* **15**, 1084–1089 (2016).
6. L. Ionov, Hydrogel-based actuators: Possibilities and limitations. *Mater. Today* **17**, 494–503 (2014).
7. Y. Yu, M. Nakano, T. Ikeda, Directed bending of a polymer film by light. *Nature* **425**, 145 (2003).
8. F. Carpi, S. Bauer, D. De Rossi, Stretching dielectric elastomer performance. *Science* **330**, 1759–1761 (2010).
9. E. Acome, S. K. Mitchell, T. G. Morrissey, M. B. Emmett, C. Benjamin, M. King, M. Radakovitz, C. Keplinger, Hydraulically amplified self-healing electrostatic actuators with muscle-like performance. *Science* **359**, 61–65 (2018).
10. S. A. Morin, R. F. Shepherd, S. W. Kwok, A. A. Stokes, A. Nemiroski, G. M. Whitesides, Camouflage and display for soft machines. *Science* **337**, 828–832 (2012).
11. Y. Kim, H. Yuk, R. Zhao, S. A. Chester, X. Zhao, Printing ferromagnetic domains for untethered fast-transforming soft materials. *Nature* **558**, 274–279 (2018).
12. W. Hu, G. Z. Lum, M. Mastrangeli, M. Sitti, Small-scale soft-bodied robot with multimodal locomotion. *Nature* **554**, 81 (2018).
13. R. Pelrine, R. Kornbluh, Q. Pei, J. Joseph, High-speed electrically actuated elastomers with strain greater than 100%. *Science* **287**, 836–839 (2000).
14. J. Huang, S. Shian, Z. Suo, D. R. Clarke, Maximizing the energy density of dielectric elastomer generators using equi-biaxial Loading. *Adv. Funct. Mater.* **23**, 5056–5061 (2013).
15. S. J. A. Koh, C. Keplinger, T. Li, S. Bauer, Z. Suo, Dielectric elastomer generators: How much energy can be converted? *IEEE ASME Trans. Mechatron.* **16**, 33–41 (2011).
16. P. Polygerinos, Z. Wang, K. C. Galloway, R. J. Wood, C. J. Walsh, Soft robotic glove for combined assistance and at-home rehabilitation. *Rob. Auton. Syst.* **73**, 135–143 (2015).
17. Y. Kim, G. A. Parada, S. Liu, X. Zhao, Ferromagnetic soft continuum robots. *Sci. Robot.* **4**, eaax7329 (2019).
18. T. Xu, J. Zhang, M. Salehizadeh, O. Onaizah, E. Diller, Millimeter-scale flexible robots with programmable three-dimensional magnetization and motions. *Sci. Robot.* **4**, eaav4494 (2019).
19. S. W. Jin, J. Park, S. Y. Hong, H. Park, Y. R. Jeong, J. Park, S.-S. Lee, J. S. Ha, Stretchable loudspeaker using liquid metal microchannel. *Sci. Rep.* **5**, 11695 (2015).
20. R. Guo, L. Sheng, H. Gong, J. Liu, Liquid metal spiral coil enabled soft electromagnetic actuator. *Sci. China Technol. Sci.* **61**, 516–521 (2018).
21. M. D. Dickey, Stretchable and soft electronics using liquid metals. *Adv. Mater.* **29**, 1606425 (2017).
22. R. M. Alexander, H. C. Bennet-Clark, Storage of elastic strain energy in muscle and other tissues. *Nature* **265**, 114–117 (1977).
23. R. Guo, H. Wang, X. Sun, S. Yao, H. Chang, H. Wang, J. Liu, Y. Zhang, Semiliquid metal enabled highly conductive wearable electronics for smart fabrics. *ACS Appl. Mater. Interfaces* **11**, 30019–30027 (2019).
24. T. Li, Z. Zou, G. Mao, X. Yang, Y. Liang, C. Li, S. Qu, Z. Suo, W. Yang, Agile and resilient insect-scale robot. *Soft Robot.* **6**, 133–141 (2018).
25. L. Zhu, B. Wang, S. Handschuh-Wang, X. Zhou, Liquid metal–based soft microfluidics. *Small* **16**, 1903841 (2020).
26. F. Ilievski, A. D. Mazzeo, R. F. Shepherd, X. Chen, G. M. Whitesides, Soft robotics for chemists. *Angew. Chem. Int. Ed.* **50**, 1890–1895 (2011).
27. J. Duan, X. Liang, K. Zhu, J. Guo, L. Zhang, Bilayer hydrogel actuators with tight interfacial adhesion fully constructed from natural polysaccharides. *Soft Matter* **13**, 345–354 (2017).
28. M. Behl, K. Kratz, J. Zotzmann, U. Nöchel, A. Lendlein, Reversible bidirectional shape-memory polymers. *Adv. Mater.* **25**, 4466–4469 (2013).
29. Z. Ren, W. Hu, X. Dong, M. Sitti, Multi-functional soft-bodied jellyfish-like swimming. *Nat. Commun.* **10**, 2703 (2019).
30. M. Sitti, Voyage of the microrobots. *Nature* **458**, 1121–1122 (2009).

Acknowledgments: We thank A. Heiden for the technical assistance in printing molds and Z. Yu for discussions about liquid metal. **Funding:** This work was supported by the ERC Starting Grant "GEL-SYS" under grant agreement no. 757931 and a startup funding of the LIT (Linz Institute of Technology) "Soft Electronics Laboratory" under grant no. LIT013144001SEL.
Author contributions: G.M. conceived the project and designed the actuators. G.M., M.K.-M., and M.D. fabricated the actuators. G.M. developed the theoretical and numerical model for the actuators and conducted the analysis. G.M., M.D., and M.K. designed the experiments. G.M., M.D., T.S., and R.S. built the experimental setup. G.M, M.D., and T.S. conducted the experiments

and characterized the performance of the actuator. G.M. and M.D. designed the control system and programmed the code. G.M., M.D., and M.K. analyzed the result. G.M., D.W., M.D., and M.K. designed figures and videos and wrote the manuscript. All authors contributed to editing the manuscript. M.K. supervised the research. **Competing interests:** The authors declare that they have no competing interests. **Data and materials availability:** All data needed to evaluate the conclusions in the paper are present in the paper and/ or the Supplementary Materials. Additional data related to this paper may be requested from the authors.

Submitted 2 April 2020
Accepted 26 April 2020
Published 26 June 2020
10.1126/sciadv.abc0251

Citation: G. Mao, M. Drack, M. Karami-Mosammam, D. Wirthl, T. Stockinger, R. Schwödiauer, M. Kaltenbrunner, Soft electromagnetic actuators. *Sci. Adv.* **6**, eabc0251 (2020).